nature materials

Article

https://doi.org/10.1038/s41563-024-02019-3

Jamming of nephron-forming niches in the developing mouse kidney creates cyclical mechanical stresses

Received: 16 September 2022

Accepted: 11 September 2024

Published online: 09 October 2024

Check for updates

Louis S. Prahl (12,10), Jiageng Liu (13,10), John M. Viola 1,3,10, Aria Zheyuan Huang 1,3, Trevor J. Chan 1, Gabriela Hayward-Lara 4, Catherine M. Porter, Chenjun Shi⁵, Jitao Zhang © ⁵ & Alex J. Hughes © ^{1,2,3,4,6,7,8,9}

Urinary collecting tubules form during kidney embryogenesis through the branching of the ureteric bud epithelium. A travelling mesenchyme niche of nephron progenitor cells caps each branching ureteric bud tip. These 'tip domain' niches pack more closely over developmental time and their number relates to nephron endowment at birth. Yet, how the crowded tissue environment impacts niche number and cell decision-making remains unclear. Here, through experiments and mathematical modelling, we show that niche packing conforms to physical limitations imposed by kidney curvature. We relate packing geometries to rigidity theory to predict a stiffening transition starting at embryonic day 15 in the mouse, validated by micromechanical analysis. Using a method to estimate tip domain 'ages' relative to their most recent branch events, we find that new niches overcome mechanical resistance as they branch and displace neighbours. This creates rhythmic mechanical stress in the niche. These findings expand our understanding of kidney development and inform engineering strategies for synthetic regenerative tissues.

Tissue-building processes during embryonic kidney development set the lifetime number of nephrons and urinary collecting ducts in the adult organ¹. Starting at embryonic day (E)10.5 in the mouse, the ureteric bud (UB) epithelium branches into the adjacent metanephric mesenchyme to form the future collecting ducts. UB tubule tips lie at the organ surface during branching and are surrounded by dynamic clusters of cap mesenchyme cells that proliferate and serve as nephron progenitors²⁻⁴. Nephron progenitors periodically condense into future nephrons within 'armpit' regions beneath UB tips⁵⁻⁷ (Fig. 1a and Supplementary Video 1). While these events have been characterized

anatomically and molecularly^{8,9}, less is known about temporal coordination between UB branching, niche geometry and mechanics, and nephron condensation. This is because single-cell RNA sequencing (scRNA-seq), imaging and mechanics data have not yet been registered to the niche branching 'life cycle'. Linked measurements of these features are necessary to develop models of how nephron formation is initiated in vivo and in engineered systems.

We recently found that competition between UB tip repulsion and crowding within a limited surface area partially predicted mouse embryonic kidney niche geometry¹⁰. Preliminary analysis of UB tip

Department of Bioengineering, University of Pennsylvania, Philadelphia, PA, USA. Center for Soft and Living Matter, University of Pennsylvania, Philadelphia, PA, USA. ³Bioengineering Graduate Group, University of Pennsylvania, Philadelphia, PA, USA. ⁴Cell and Molecular Biology Graduate Group, University of Pennsylvania, Philadelphia, PA, USA. 5Department of Biomedical Engineering, Wayne State University, Detroit, MI, USA. 6Department of Cell and Developmental Biology, University of Pennsylvania, Philadelphia, PA, USA. 7Center for Precision Engineering for Health (CPE4H), University of Pennsylvania, Philadelphia, PA, USA. 8 Materials Research Science and Engineering Center (MRSEC), University of Pennsylvania, Philadelphia, PA, USA. 9Institute for Regenerative Medicine, University of Pennsylvania, Philadelphia, PA, USA. 10These authors contributed equally: Louis S. Prahl, Jiageng Liu, John M. Viola. e-mail: ajhughes@seas.upenn.edu

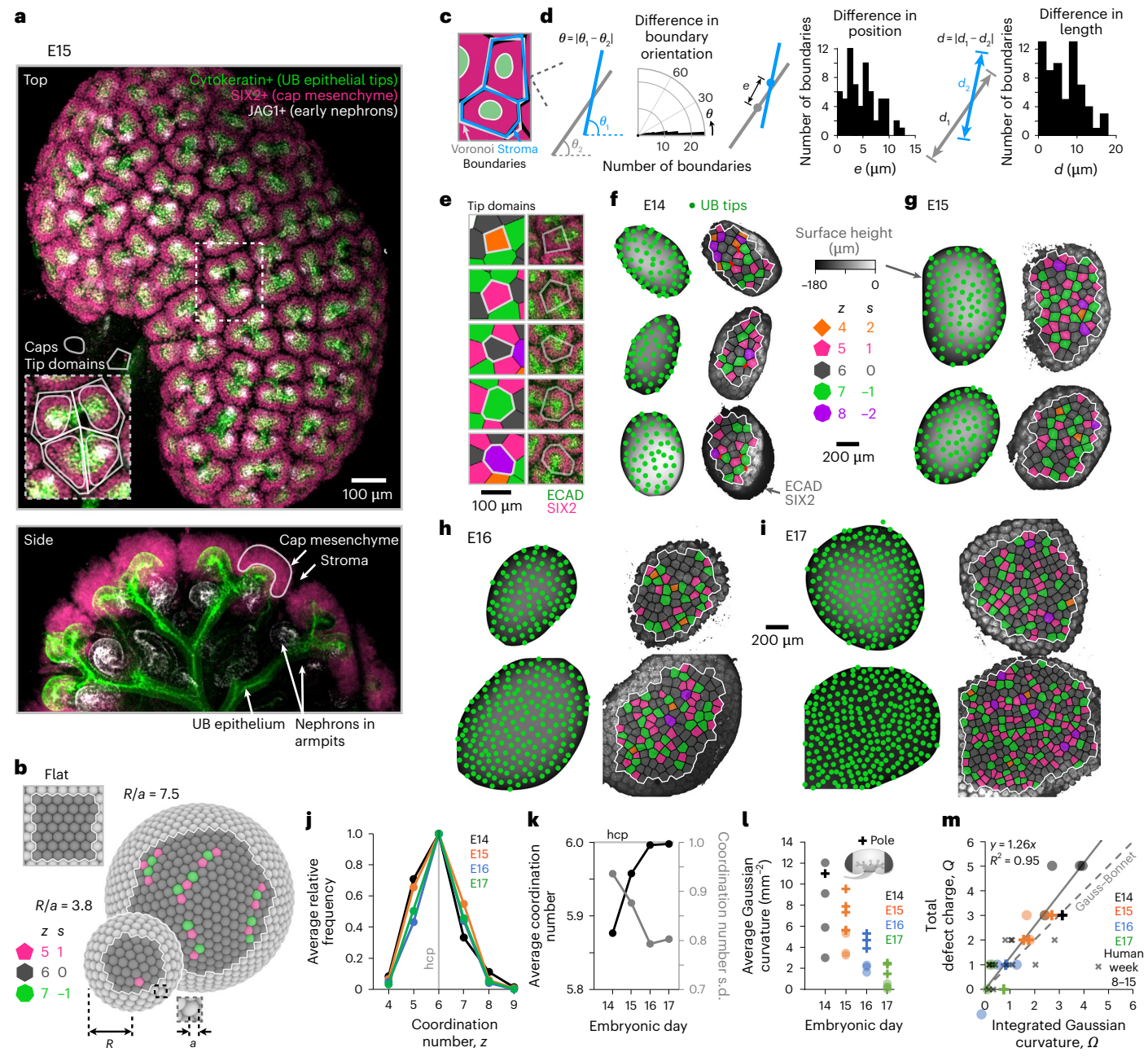


Fig. 1 | Kidney curvature imposes topological requirements on geometry of close-packed nephrogenic niches at UB epithelial tubule tips. a, Whole-mount confocal immunofluorescence maximum projection (top) and xz plane (bottom) for E15 mouse kidney. Branching cytokeratin+ UB tubule tips are surrounded by SIX2+ nephron progenitors in the cap mesenchyme. Caps are separated by thin ribbons of stroma (unlabelled). JAG1+ early nephrons form at 'armpits' beneath tubule tips. We define 'tip domains' by Voronoi polygons. The inset shows a zoomed-in view of the area in the dashed box. **b**, Model of repulsive particle (radius a) packing at the surface of a sphere (radius R), showing pentagonal and heptagonal topological defects among an otherwise hexagonal packing. Defects form pairs, clusters or chains for R/a > 5. c, Schematic of overlap between Voronoi and tip domain stromal interfaces. d, Plots of difference between Voronoi and stromal interface segment orientation (θ) , midpoint position (e)and length (d). **e**, Example Voronoi cells used to define tip domain interfaces overlaid on confocal micrographs. f-i, UB tip positions overlaid on height maps of representative kidney surfaces over E14-E17 (left). Voronoi diagrams tracing tip domains on micrographs of combined ECAD and SIX2 immunofluorescence

(right). Voronoi cells are coloured by coordination number (the number of neighbours). \mathbf{j} , Frequency plot of tip domain coordination number (n = 162, 353,535 and 892 tip domains in E14, E15, E16 and E17 stages across 5, 6, 4 and 4 kidneys, respectively). The grey line indicates hexagonal close packing (hcp), which occurs at a coordination number of 6. k, Average and standard deviation (s.d.) of coordination number distributions. I, Average Gaussian curvature for patches of kidney surface at poles and non-poles; n = 5, 8, 6 and 7 poles or kidneys in the E14, E15, E16 and E17 stages, respectively. \mathbf{m} , Sum (Q) of topological charges (s; net decrease in coordination number from z = 6) against integrated Gaussian curvature (Ω) for patches of mouse embryonic kidney surface at poles and non-poles, and human embryonic kidney surface (units of disclinations); n = 5, 6,4 and 4 poles or kidneys in the E14, E15, E16 and E17 mouse stages, respectively, and n = 3, 3, 4 and 3 patches across 3, 2, 3 and 2 kidneys in the week 8, 11, 13 and 15 $human\,stages, respectively.\,Human\,kidney\,data\,are\,a\,reanalysis\,of\,images\,from$ ref. 22; details in Supplementary Fig. 2. R2 is the coefficient of determination The dotted line represents the Gauss-Bonnet theorem (Supplementary Note 3).

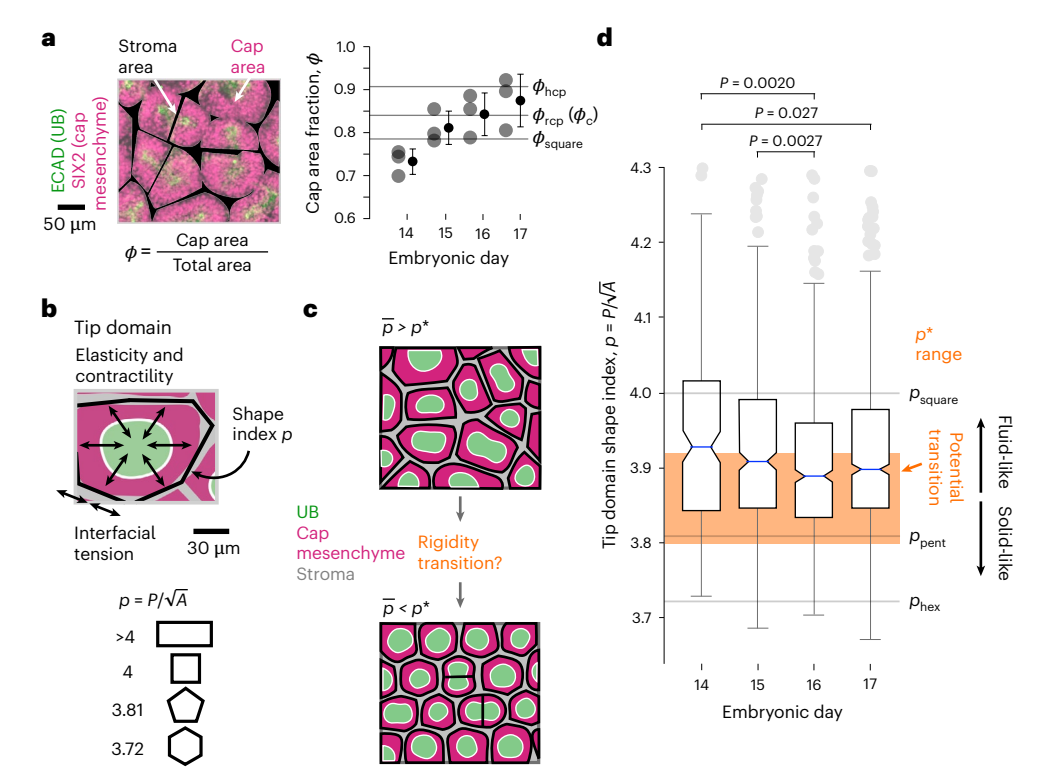


Fig. 2 | **Close packing of UB tip domains predicts a transition to rigidity over developmental time. a**, Segmented confocal micrograph indicating the area fraction ϕ of cap mesenchyme (left). Plot of ϕ over developmental time (transparent black points), relative to horizontal lines indicating 2D square packing (ϕ_{square}), random close packing (ϕ_{rcp}) and hexagonal close packing (ϕ_{hcp}) of circles (right). Solid black points are mean \pm s.d., n=3 kidneys per embryonic day, points averaged over >12 tip domains per kidney. Note that $\phi_{\text{rcp}} = \phi_{\text{c}}$ for 2D circle packing, **b**, Definition of shape index of tip domains p from Voronoi cell

perimeter (P) and area (A). \mathbf{c} , Schematic of density-independent stiffening or rigidity transition when median shape index \bar{p} drops into a critical range below p^* . \mathbf{d} , Box and whisker plots of tip domain shape index distributions over time, relative to those for squares (p_{square}), pentagons (p_{pent}) and hexagons (p_{hex}), and to $p^*=3.8-3.92$ (n=177,391,617 and 987 tip domains in E14, E15, E16 and E17 categories across 5, 6, 4 and 4 kidneys, respectively). One-way analysis of variance (ANOVA) and Tukey's test were used. Horizontal lines are minimum and maximum (excluding outliers), and quartiles (25/50/75%); points are outliers.

positions revealed local ordering in crystal-like packing geometries. These observations suggested an analogy to two-dimensional (2D) curved crystals of repulsive particles^{11–15}. Crystal-like niche packing could impact the developmental trajectory of the kidney by setting limits on tip domain density (and therefore nephron number) for a given organ surface area. Physical microenvironmental changes dictated by curved crystal physics during niche branching cycles could also affect nephron progenitor decision-making (Supplementary Note 1).

Here we combine the theory of curved crystals, rigidity in close-packed systems and force inference with micromechanical analysis to characterize nephrogenic zone geometry and mechanics. We then register the properties of individual niches to the UB branching life cycle. Our data reveal that niche packing drives a transition from more fluid-like to more solid-like mechanics that enable sustained stresses between nephrogenic niches after -E15. This in turn causes rhythmic cycles of stress within them that are synchronized with the UB branching life cycle.

Kidney curvature influences ureteric bud tubule geometry

UB tubule tips branch just beneath the organ surface. Each tip is surrounded by a swarm of 'cap' mesenchyme cells that serve as nephron progenitors. These tip domain niches repel one another '1.16.17', creating dense arrays separated by thin 'ribbons' of stroma (Fig. 1a and Supplementary Video 1). We previously hypothesized an analogy for the close packing of niches in the physics of repulsive or elastic particles at surfaces '0', but had not previously considered the effect of curvature '15.18,19'. Repulsive particles undergo hexagonal close packing

(triangular packing) on a flat surface so that each particle has six neighbours (that is, the coordination number z=6; Fig. 1b). Wrapping a triangular lattice onto a doubly curved surface (that is, a surface with non-zero Gaussian curvature) favours 'disclination' topological defects that increase or decrease z. For example, a soccer ball is not made up of hexagonal patches but rather a mixture of hexagonal (z=6) and pentagonal (z=5) patches. For large curved crystals, isolated disclinations are less favourable and are replaced by pairs (dislocations), clusters or chains ('scars'; Supplementary Note 2 and the literature (1,12,14). We therefore wondered if UB tip positions adhere to the same topological requirements.

We generated Voronoi tessellations from annotated UB tip positions on E14–E17 kidneys to predict the lattice boundaries of each tip 'domain' (all UB epithelium, cap mesenchyme and stroma that are closer to a given tip than to a neighbouring one; Fig. 1c). Voronoi edges overlapped stromal interfaces between domains, indicating that they carry physical meaning. To quantify this overlap, we annotated stromal interface segments and found only small mismatches in their orientations $(5.5\pm4.4^\circ,$ mean \pm s.d., n = 64 segments), midpoint positions $(5.8\pm3.0~\mu\text{m})$ and lengths $(6.8\pm4.7~\mu\text{m})$ relative to the corresponding Voronoi edges (Fig. 1d). A similar correspondence exists in 2D foams and confluent cell layers 20,21 , implying that the size and shape of tip domains are restricted by the presence of neighbouring ones. These data show that tessellated polygons accurately approximate stromal interfaces between tip domains.

The theory of curved crystals suggests that the degree of bias towards pentagon disclinations will increase linearly with curvature (Supplementary Note 3). We quantified this bias using the 'topological

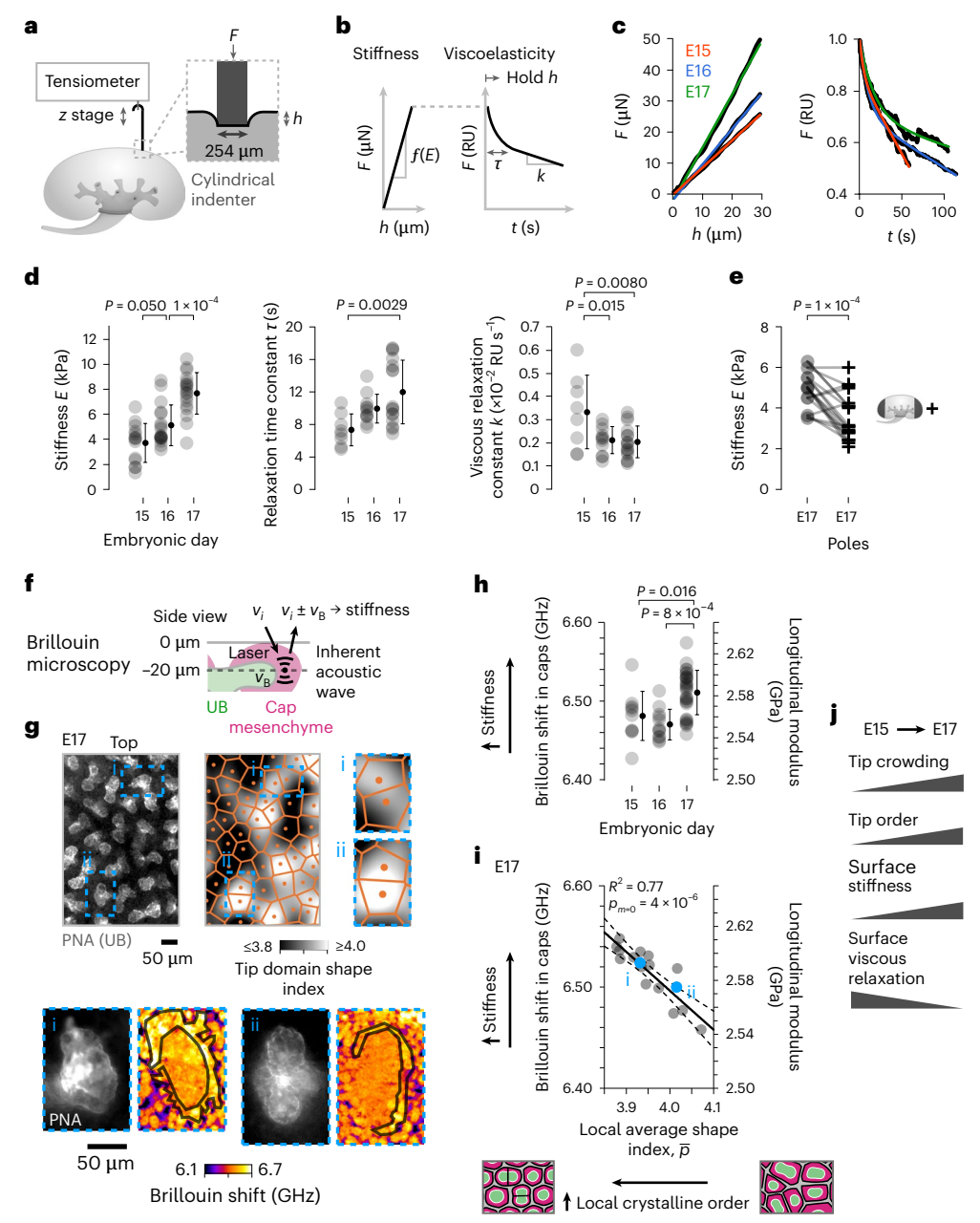


Fig. 3 | Crowding of UB tip domains stiffens the nephrogenic niche over time, especially in close-packed regions. a, Schematic of surface microindentation using cylindrical indenter (F, indentation force) that captures kidney viscoelastic properties on length scale of about three tip domains for an indentation depth h of ~30 µm. b, Schematic of typical data output and key parameters during indentation (left) and during subsequent recording of force at fixed final indentation depth (right). f(E) indicates a function of stiffness (see Methods). RU: relative units c, Representative indentation force versus indentation depth curves (left) and force relaxation curves (right) for E15-E17 kidneys. Black lines are representative experiment data, colored lines are model fits (see Methods). **d**, Stiffness E, relaxation time τ and viscous relaxation constant k plots over E15–E17 (mean \pm s.d.; n = 14, 17 and 18 kidneys for stiffness and n = 8, 11 and 16 kidneys for τ and k for E15, E16 and E17, respectively; one measurement per kidney). RU, relative units. e, Stiffness plots for paired measurements of E17 kidneys and their poles (n = 19 measurement pairs over 12 kidneys, 1–2 pairs per kidney, paired two-tailed t-test). **f**, Schematic of Brillouin microscopy. v_i is the

incident light frequency and v_b is the Brillouin frequency shift. \mathbf{g} , Live confocal micrograph of Alexa Fluor 488-PNA-labelled UB tips, Voronoi diagram of tip domains with heat map of shape index and zoomed insets of two example domains (top). PNA, peanut (Arachis hypogaea) agglutinin lectin. Insets of the two example domains with PNA fluorescence and Brillouin shift images (bottom). Cap mesenchyme cells local to tips are outlined. h, Mean Brillouin shift in caps over E15–E17 (mean \pm s.d., n = 10, 12 and 29 tip domains for E15, E16 and E17 across 6,7 and 15 kidneys, respectively). i, Mean Brillouin shift and corresponding estimated longitudinal modulus in cap mesenchyme cells versus average tip domain shape index in their local neighbourhood of approximately three tips (n = 17 tip domains across four E17 kidneys). Fit line from linear regression analysis is shown with 95% confidence interval envelope and p value testing the null hypothesis that slope m = 0 ($p_{m=0}$). At bottom, sketch of niche packing/ crystalline order interpretation of local average shape index axis. j, Summary of changes in UB tip geometry and kidney surface mechanics over E15-E17. Statistics in d and h are one-way ANOVA and Tukey's test.

charge's of tip domains, given by the formula s = 6 - z (Fig. 1b,e,f). We separately reconstructed the associated kidney surfaces from three-dimensional (3D) confocal images to generate curvature maps (Supplementary Fig. 1; overlays in Fig. 1f-i). Tip coordination numbers

varied between 4 and 8, and tip patterns qualitatively transitioned from a disordered state at E14–E15 to a more visually apparent local order at E16–E17 (more information is in the literature 10). The median coordination number was z = 6, with a bias towards lower coordination

numbers at earlier developmental times (Fig. 1j). At later times, the coordination number distribution approached a mean of 6, consistent with hexagonal packing on flat surfaces (Fig. 1k). This is consistent with tip patterns adopting energetically favourable pentagon disclinations (that is, tips with z = 5 neighbours instead of 6) in younger kidneys that have higher curvature (Fig. 11,m). Kidney poles had higher curvature than non-pole regions at each developmental stage (Fig. 11), but both followed the same topological charge versus curvature trend (Fig. 1m). This indicates that curvature is a better predictor of tip domain packing than developmental stage, though crowding-dependent effects also contribute (more information is in the following section and the literature¹⁰). Variation in tip domain size and shape accounted for most 'excess' dislocations (Supplementary Note 2). But we also saw evidence of grain boundary scars and defect clusters of alternating charge, as occur in other large, curved crystals (Fig. 1f-i)11,12,14. These data show that topological limitations imposed by kidney curvature influence tip packing geometry.

To extend this result, we reanalysed published confocal immunofluorescence stacks from human embryonic week 8-23 kidneys (Supplementary Fig. 2 and the literature 22). Human kidneys have a multilobed structure 22 , but the tip domains in lobes can be analysed using the same Voronoi boundary approach (Supplementary Fig. 2a-d). Despite the species difference, human data followed the same total topological charge versus curvature relationship as mouse kidneys and poles (Fig. 1m and Supplementary Fig. 2e). This indicates that curvature similarly affects both mouse and human tip domain organization.

Crystal-like tubule packing creates a rigidity transition

Crowding can drive abrupt changes in the geometric and mechanical properties of elastic particles¹⁸, foams and emulsions²³, and cells in tissues²⁴. We hypothesized that tip domain crowding would have similar effects in the nephrogenic zone of the embryonic kidney. During branching morphogenesis, UB tips, cap mesenchymes and stromal ribbons are fluid-like on the timescale of tip branching (Supplementary Note 4). An excess rate of new tip formation and the thinning of stromal boundaries over E14-E18 (refs. 3,10) cause niches to pack closely and conform in shape due to confinement from neighbouring niches. We also previously reported regions of local tip domain alignment¹⁰, another feature of packed systems. Tip domain collectives have features of both non-confluent (density-dependent) and confluent (density-independent) packing due to the presence of stromal interfaces. We applied both areas of theory separately to gain insight on packing mechanics. Density-dependent packing theory predicts a rigidity (jamming) transition when particles exceed a critical packing fraction ϕ_c . Here, yield stress transitions from zero to a finite value (that is, from fluid-like to solid-like behaviour)^{24,25}. For kidney caps, we measured the packing fraction ϕ on a 2D basis as the ratio of cap area to total area. The ϕ values exceeded those for 2D body-centred (square) packing of circles and random close packing (which defines the critical area fraction ϕ_c ; refs. 25,26), and even approached that for 2D hexagonal close packing from E15-E17 (Fig. 2a). In human embryonic kidney lobes, ϕ exceeded ϕ_c from at least week 11 to week 18 (Supplementary Fig. 2f). Week 11 is notable since kidneys at this stage are similar in size, curvature and niche architecture to the E15-E17 mouse kidney (compare Fig. 1 and Supplementary Fig. 2; more information is in the literature²²). The ϕ value then dropped below ϕ_c sometime between week 18 and week 23, where tip/niche architecture is reminiscent of the later postnatal day 2 mouse kidney²². This predicts a jamming transition, such that the 'nephrogenic zone' as a whole is predicted to be solid-like and therefore capable of imposing mechanical stress on newly formed niches during tip branching after ~E15 in mice and ~week 11 in humans.

Although ϕ predicts density-dependent jamming of niches, the underlying theory neglects potentially important parameters (Supplementary Note 5). We therefore applied density-independent rigidity

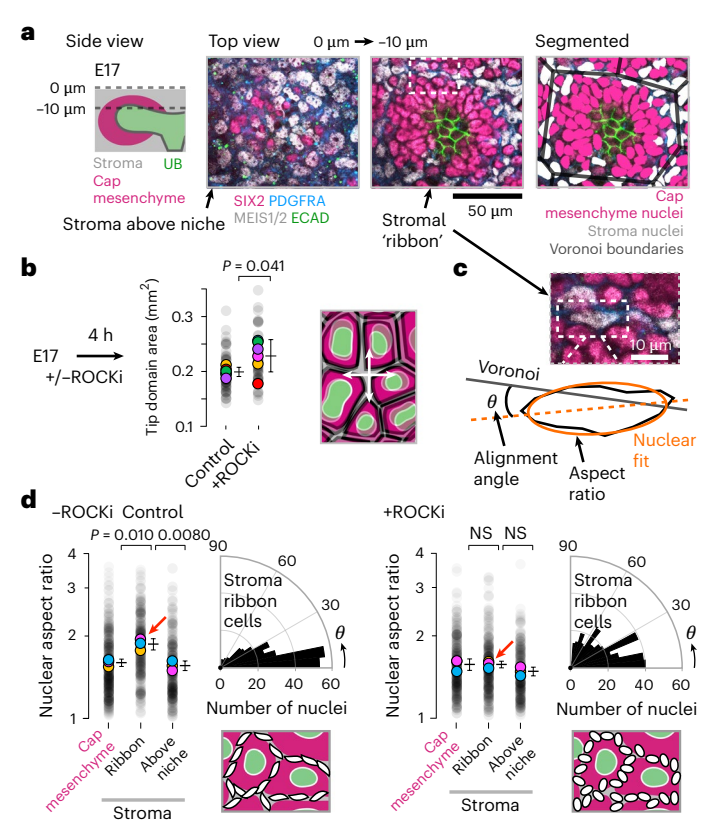


Fig. 4 | Domain size and stromal cell elongation and alignment at ribbon interfaces between domains is dependent on myosin II. a, Schematic showing side (xz) view of a tip domain (left). Top-view confocal immunofluorescence micrographs at the organ surface and 10 µm deeper into an E17 kidney at the tip plane (right), **b**. At left, tip domain areas for E17 kidneys incubated for 4 h in the presence (+ROCKi) or absence (control) of 30 µM ROCKi Y-27632 (n = 63 and 52 domains for control and +ROCKi, respectively, across six kidneys per condition). Transparent black points are tip domains, whereas coloured points are means per kidney, and mean ± s.d. is shown for each kidney mean. At right, schematic of tip domain area increase in response to ROCKi. c, At top, immunofluorescence micrograph of example stromal ribbon. At bottom, schematic of nuclear aspect ratio and alignment to nearest tip domain Voronoi boundary. d, Cap mesenchyme and stromal cell nuclear aspect ratio (at tip plane and 'above niche'), and stroma ribbon cell nuclear alignment to nearest Voronoi boundary for E17 kidneys incubated for 4 h in the presence or absence of 30 uM ROCKi (for the nuclear aspect ratio, n = 165.103 and 92 cells for -ROCKi categories from left to right, and n = 116, 113 and 107 cells for +ROCKi categories from left to right, across three kidneys per condition; for the nuclear alignment, n = 271and 338 cells for -ROCKi and +ROCKi, respectively, across three kidneys per condition). Transparent black points are nuclei, whereas coloured points are means per kidney, with mean \pm s.d. shown for each kidney mean. Red arrows added for emphasis. Schematics at bottom visually summarize stromal cell nuclei elongation and alignment data. Statistics in **b** and **d** are unpaired two-tailed t-tests on kidney means. NS, not significant.

theory created for the high packing fraction regime that accounts for these parameters. Since niches pack side to side in one layer, we turned to a family of 2D vertex and Voronoi models developed for tissues organized into tessellated polygonal subunits having elasticity, contractility and interfacial tension $^{27-31}$ (Supplementary Note 5). For any subunit with these properties, such as individual cells or tip domains, the models predict substantial stiffening or a sharp transition to rigidity when the median (\bar{p}) of a geometric parameter of their boundaries called the shape index p drops below a critical value p^* in the range of 3.8–3.92 (Fig. 2b,c; refs. 30,31). For sharp transitions, when $\bar{p} > p^*$, no energy barrier exists to changes in packing configuration, conferring fluid-like mechanics. However, when $\bar{p} < p^*$ the configuration of poly-

gons has both bulk and shear stiffnesses, conferring solid-like mechanics²⁸. To apply the model to the kidney, we measured the shape indices of tip domains over E14-E17, finding that the median shape index significantly decreased with developmental time, dropping into the critical range below 3.92 after ~E15 (Fig. 2d). The same trend held in human embryonic kidney lobes, where median shape index dropped into this range at -week 11 (Supplementary Fig. 2g), again a stage similar to ~E15–E17 in the mouse²². The change in shape index here is in a similar range to that previously associated with a rigidity transition in airway epithelial tissues in vitro²⁹. We note that flattening of the kidney surface as it grows could also reinforce the transition by increasing the critical shape index at which rigidification occurs³². These results suggested that tip domain collectives may become stiffer and have less viscous behaviour after E15, consistent with the time at which semi-crystalline order begins to appear (Fig. 1, Supplementary Figs. 2h and 3, Supplementary Note 6, Supplementary Video 2a and the literature¹⁰).

Temporally, the overall decrease in p and increase in tip domain crystalline order predict increased tissue stiffness over time. Spatially, local regions of higher crystalline order (lower local average p) should be stiffer at a given time. We next assayed tissue mechanics over time and space to test this. We measured the Young's modulus (stiffness, E) and viscoelasticity of freshly dissected E15-E17 kidneys by microindentation with a 254 µm cylindrical indenter (equivalent to the width of approximately three tip domains; Fig. 3a and the Methods). We measured the applied force during indentation of the kidney surface by ~30 μm (that is, the elastic component), and paused indentation to capture the time dependence of force during subsequent tissue relaxation (that is, the viscous component; Fig. 3b,c). These measurements first revealed a 110% increase in kidney surface stiffness local to tip domains over E15-E17 (Fig. 3d). Second, they showed a decrease in viscous relaxation k and an increase in the relaxation timescale τ . These data reveal a marked stiffening and decrease in viscous behaviour over E15-E17-the same period over which our tip domain shape index analysis predicted a fluid-like to solid-like rigidity transition (Fig. 2d).

An alternative hypothesis here is that kidney maturation drives stiffening, rather than tip domain jamming. To test this, we reasoned that kidney pole regions would have tip packing topologies resembling earlier developmental stages due to their higher curvature. This would make poles softer and give them increased viscous behaviour compared to non-pole regions. Indeed, we found that the indentation mechanics of E17 poles were comparable to E15/E16 non-pole regions rather than E17 ones (Fig. 3e and Supplementary Fig. 4). This result argues against the alternative hypothesis that tissue mechanics change primarily as a function of developmental maturation.

Local tip domain regions with higher order should be stiffer, producing spatial variation at a given developmental stage. Microindentation

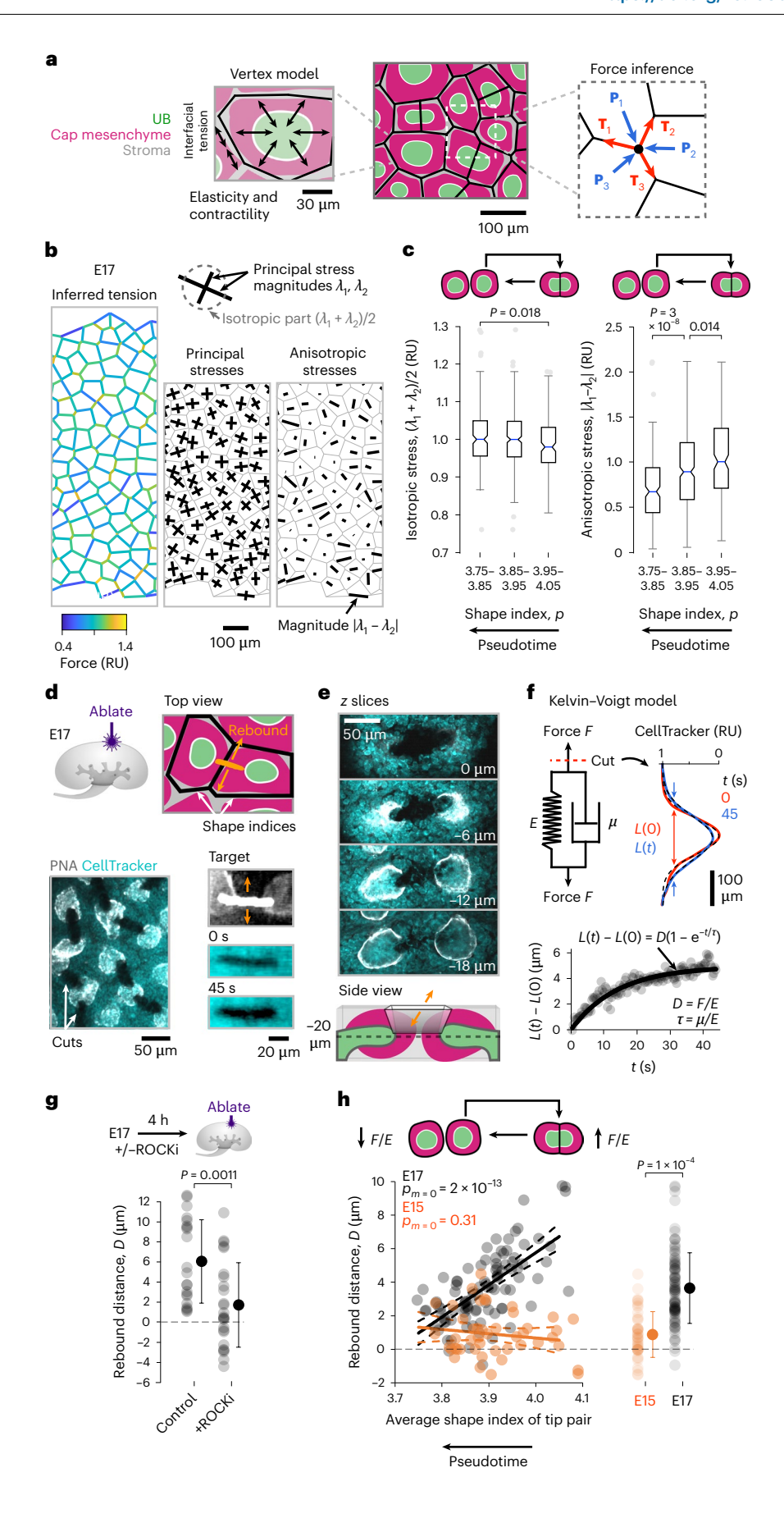
did not permit correlating local tip packing states to mechanics data. We instead used confocal Brillouin microscopy³³, a label-free optical technique previously used to quantify the mechanics of developing tissues^{34–36}. Brillouin microscopy measures the frequency shift between incident and scattered light (Fig. 3f and the literature³⁷). This Brillouin shift scales with the high-frequency longitudinal modulus, which is proportional to E (Supplementary Fig. 5 and Supplementary Note 7). We acquired 2D Brillouin images of E15-E17 tip domains at planes approximately bisecting UB tip domains, and averaged the Brillouin shift within each cap mesenchyme (Fig. 3g). These shifts significantly increased between E15/E16 and E17 (Fig. 3h), similar to the microindentation trend in Fig. 3d. In E17 kidneys, we further found that the Brillouin shift in caps and the average shape index in a local neighbourhood of about three tips were negatively correlated (Fig. 3i). Specifically, the longitudinal modulus of the cap mesenchyme is higher for tip domains predicted to reside in more closely packed and solid-like regions. The data predict a stiffness increase in the cap mesenchyme of ~19% from E16-E17 (compared to 50% by microindentation) and a range of ~53% among niches in different local packing states at E17 (Supplementary Note 7). These data show that the stiffness variation among nephrogenic niches due to the tip packing state is substantial and on a similar order of magnitude as the increase over developmental time (Fig. 3j).

Defining a life cycle for asynchronous branching

Our mechanics data advance a model where increasing surface stiffness and decreased viscous behaviour would increase the mechanical resistance to new tips branching and displacing close-packed neighbours (Supplementary Video 2b). Since branching of UB tips is asynchronous, establishing a life cycle estimate would enable registration of stress measurements from different niches to a common 'pseudotime'. Creating a pseudotime axis is necessary because it is not currently possible to perform live time-lapse imaging of tip branching in kidney explants while retaining the in vivo 3D architecture of the organ³⁸. We reasoned that tips bearing more nephrons should be 'older' relative to their last branching event, since nephrons are distributed among daughter tips when a tip divides³. We found that recently divided tips bearing fewer nephrons had a lower area and higher shape index, while older tips bearing more nephrons were larger with a lower shape index (Supplementary Figs. 6 and 7 and Supplementary Note 8). These data imply that the tip domain shape index can be used as a pseudotime metric to register tips with respect to their stage in the branching process. Plotting nephron number per tip versus branching pseudotime was sensitive enough to detect an apparent pause in nephrogenesis early in the branching initiation, highlighting the flexibility of the pseudotime concept to register anatomical, molecular³⁹ and other data (Supplementary Figs. 6 and 7 and Supplementary Note 8).

 $Fig.\,5\,|\,Newly\,established\,tip\,domains\,experience\,an isotropic\,mechanical$ stress that decreases over each life cycle. a, Schematic of contributions to tension (T) and pressure (P) forces that balance at Voronoi vertex nodes. b, Example force inference output from Voronoi geometry overlaid on E17 kidney surface confocal fluorescence micrograph. Principal stresses (maximum and minimum) are shown with lengths proportional to their eigenvalues (magnitudes) λ_1 and λ_2 . The anisotropic stress tensor is shown as one bar representing the tension part (Methods). c, Box and whisker plots of normalized isotropic and anisotropic stress at tip domains (n = 195, 319 and 164 tip domains in low, medium and high shape index categories, respectively, across four kidneys; one-way ANOVA, Tukey's test). Horizontal lines are minimum and maximum (excluding outliers), and quartiles (25/50/75%); points are outliers. Diagrams above the plots indicate a branching life-cycle interpretation of the pseudotime axis. d, Laser microdissection schematic showing ablation between neighbouring tip domains at E17 (top). Example cuts imaged by confocal microscopy after fixation, and live wide-field micrographs of one target cut showing the intended cut location (white line) before ablation, and at 0 s and 45 s after ablation (bottom). e, Serial confocal z slices after fixation

(top), showing penetration of cut ~20 µm through inter-tip region (cell integrity disrupted down to ~40 µm). Schematic of cut penetration relative to typical niche anatomy (bottom). f, Kelvin-Voigt model. The top left shows spring (stiffness E) and dashpot (viscosity μ) elements that determine cut opening properties in response to tissue tension. The top right plot shows Gaussian fits (dotted lines) to the cut fluorescence for each timepoint. The bottom shows the cut opening distance fitted with the model, yielding the asymptotic cut opening distance D and time constant τ . **g**, Cut rebound for 4 h E17 kidney incubation in presence or absence (control) of 30 μ M ROCKi Y-27632 (mean \pm s.d., n = 21 and 25 cuts for control and +ROCKi, respectively, across two kidneys per condition). h, Plot of ${\it D}$ against average shape index of tip domains immediately adjacent to each cut (left; n = 45 and 96 cuts for E15 and E17 across 5 and 7 kidneys, respectively). Linear regression fits are shown with 95% confidence intervals and P values testing the null hypothesis that slope m = 0. The diagram above the plot indicates a branching life-cycle interpretation of the pseudotime axis. At the right are the distributions of all data for E15 and E17 (mean ± s.d.). Statistics in g and h (right) are unpaired two-tailed t-tests.



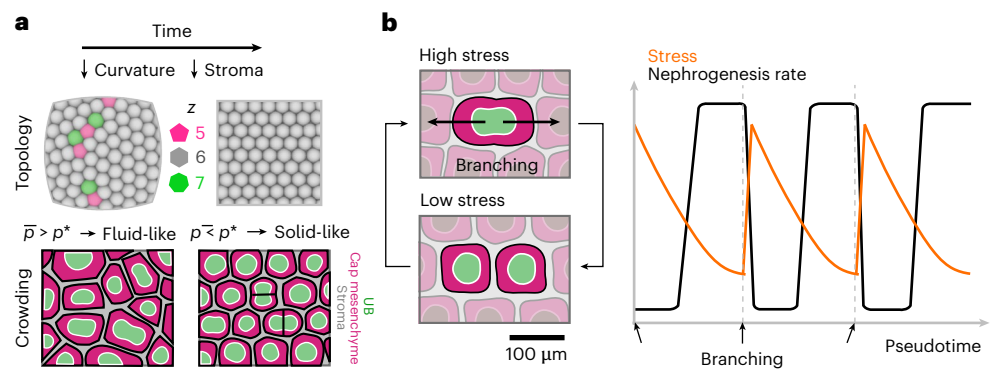


Fig. 6 | **Model for curvature and crowding contributions to nephrogenic niche packing and its effects on mechanics. a**, Schematic summary of curvature and crowding contributions to nephron-forming niche geometry and rigidity transition. **b**, Left, schematic of cyclical mechanical stress in the

niche microenvironment associated with the UB tip branching life cycle. Right, qualitative plot of the inferred temporal relationship between stress and nephrogenesis rhythms in the niche.

Branching tips experience cyclic mechanical stress

We applied our pseudotime definition to test if tip domain branching causes transient mechanical stresses between neighbouring tip domains at the intervening ribbon-like stromal interfaces (Fig. 4a), putting them under tension. In E17 kidneys, we measured a 15% increase in niche cross-sectional area after 4 hincubation with the rho-associated protein kinase (ROCK) inhibitor Y-27632 (ROCKi), relative to controls (Fig. 4b). Since ROCKi reduces cell contraction by inhibiting myosin II phosphorylation⁴⁰, the data indicate that collective cell tension is necessary to maintain normal niche size. We separately found that primary cortical stromal cells have the highest traction force and phospho-myosin light chain levels relative to UB and cap mesenchyme cells⁴¹. These data suggest that stromal interfaces between tip domains are under mechanical tension, so we looked for evidence of circumferential nuclear elongation and alignment along the boundary that would indicate anisotropic stress (Supplementary Note 9). Stromal cell nuclei appeared to align along ribbon interfaces in both E17 mouse and week 17 human kidneys (Fig. 4a,c and Supplementary Fig. 8). We found that mouse stromal cells in ribbons had an ~18% higher nuclear aspect ratio (elongation) than those sitting above the niche or neighbouring cap mesenchyme cells (Fig. 4d). This elongation relative to cells in the other compartments was lost upon 4 h kidney treatment with ROCKi. Stromal nucleus alignment along boundaries also decreased upon ROCKi treatment, from a mean deviation angle of 23° to 35° (Fig. 4d). Together the data show that tip domain size and stromal cell elongation and alignment along domain interfaces is dependent on myosin II. In other words, stromal ribbons form a tensile network counteracting effective niche pressure. Branching morphogenesis may contribute to this effective pressure.

To quantitatively relate tip branching life cycle to niche mechanical stress, we applied force inference developed for cell-scale vertex models 42 (Fig. 5a and Supplementary Note 10). Parallel (interfacial tension) and perpendicular (hydrostatic pressure, elasticity and contractility) forces are inferred from observable variations in interface edge lengths and angles. Bayesian force inference produced a map of the inferred stress tensor from E17 tip domain Voronoi edges 43 . Major and minor principal stress axes and their relative magnitudes define isotropic and anisotropic stresses (Fig. 5b and Methods). Plotting these components against p revealed that as tips age relative to their last branching event (that is, as shape index decreases), inferred anisotropic stress decreases by -30% (Fig. 5c). This predicts a rhythmic mechanical stress microenvironment synchronized with the tip life cycle, with increased anisotropic stress early in branching versus later.

To experimentally validate inferred stress predictions, we used laser microdissection of freshly dissected E15 and E17 kidneys to ablate

inter-tip regions spanning neighbouring cap mesenchyme clusters and intervening stromal ribbons (Fig. 5d, Supplementary Figs. 9 and 10 and Supplementary Video 3). Laser ablation reflects anisotropic stress at the cutting sites, and the asymptotic rebound (opening) distance of cut edges, D, equals the local tension/elasticity ratio⁴⁴. We reasoned that cuts orthogonal to stromal ribbons would report on tensile forces predicted by force inference modelling (Fig. 5a). Ablation successfully induced rebound at cut sites (Fig. 5d) comparable to other developing tissue settings (Supplementary Note 11). Cuts penetrated ~20 µm in depth, sufficient to sever the mesenchyme and stromal ribbons down to the midplane of the tip domain interfaces in the z direction (Fig. 5e). Cut opening distances over time L(t) were estimated by automated Gaussian fitting, and plots of L(t) versus t were fit with a Kelvin-Voigt model to estimate the asymptotic rebound distance D (Fig. 5f and Supplementary Fig. 9). We verified that *D* related to tissue tension by incubating E17 kidneys with ROCKi for 4 h before cutting, which significantly decreased D relative to controls (Fig. 5g). On the other hand, D significantly increased with the average shape index of tip domains adjacent to each cut at E17 (Fig. 5h and Supplementary Fig. 9e), in agreement with the force inference results. These data show that anisotropic stress local to tip domains is highest for newly branched tips (high p) and lowest for older tips (low p). This correlation held for E17 kidneys but not for E15 kidneys prior to the rigidity transition, where residual stresses would be predicted to dissipate and not be transmitted among domains (Fig. 5h). The force inference modelling and ablation data together validate that anisotropic stresses are higher in newly branched tip domains as they displace close-packed neighbours in kidneys that have crossed the rigidity transition. This local stress then dissipates prior to the next branching cycle (Supplementary Video 2b).

Outlook

Gaining a fundamental understanding of tissue-wide coordination between UB, nephron and stromal morphogenesis will improve understanding of disease-relevant variability in nephron endowment and subsequent adult kidney function^{45–47}. An emerging area of interest is to determine potential geometric and mechanical factors that may add context-dependent cues to cell decision-making in and adjacent to nephrogenic niches. These include the mutual inhibition of UB tip branching based on local crowding⁴⁸; the interplay between nephron progenitor number per tip and nephrogenesis rate⁴⁶; and the dependence of progenitor exposure to pro-renewal versus pro-differentiation ligands on niche shape and on cell migration^{7,49}.

Our work offers a fundamental characterization of nephrogenic niche geometry and mechanics over the UB tip branching life cycle (Fig. 6). Together with the observation that UB tips progressively overcrowd the kidney surface¹⁰, our data show that niches physically

compete for occupancy after -E15 in the mouse, creating measurable mechanical stress local to each branch event.

Our data set up several areas for future investigation of in vivo and in-kidney organoid models. We recently found that niches alternate between nephron progenitor renewal and differentiation phases that synchronize with branching³⁹. Our data on rhythmic mechanical stress in niches raises the question of whether these two rhythms are causally linked (Supplementary Note 1). These and other studies have inspired organoid engineering efforts seeking to advance beyond the status quo of nephron formation in a single pulse towards ongoing, periodic nephrogenesis ⁵⁰. Mimicking the rhythmic biology of the nephrogenic niche will aid these engineering efforts for regenerative medicine and yield new insight into compositional control of the kidney.

Online content

Any methods, additional references, Nature Portfolio reporting summaries, source data, extended data, supplementary information, acknowledgements, peer review information; details of author contributions and competing interests; and statements of data and code availability are available at https://doi.org/10.1038/s41563-024-02019-3.

References

- Rumballe, B. A. et al. Nephron formation adopts a novel spatial topology at cessation of nephrogenesis. *Dev. Biol.* 360, 110–122 (2011).
- Lindström, N. O. et al. Integrated β-catenin, BMP, PTEN, and Notch signalling patterns the nephron. Elife 3, e04000 (2015).
- Short, K. M. et al. Global quantification of tissue dynamics in the developing mouse kidney. Dev. Cell 29, 188-202 (2014).
- Combes, A. N., Lefevre, J. G., Wilson, S., Hamilton, N. A. & Little, M. H. Cap mesenchyme cell swarming during kidney development is influenced by attraction, repulsion, and adhesion to the ureteric tip. Dev. Biol. 418, 297–306 (2016).
- Carroll, T. J., Park, J.-S., Hayashi, S., Majumdar, A. & McMahon, A. P. Wnt9b plays a central role in the regulation of mesenchymal to epithelial transitions underlying organogenesis of the mammalian urogenital system. Dev. Cell 9, 283–292 (2005).
- Brown, A. C. et al. Role for compartmentalization in nephron progenitor differentiation. *Proc. Natl Acad. Sci. USA* 110, 4640–4645 (2013).
- Mederacke, M., Conrad, L., Doumpas, N., Vetter, R. & Iber, D. Geometric effects position renal vesicles during kidney development. Cell Rep. 42, 113526 (2023).
- Lindström, N. O. et al. Spatial transcriptional mapping of the human nephrogenic program. Dev. Cell 56, 2381–2398.e6 (2021).
- Lindström, N. O. et al. Progressive recruitment of mesenchymal progenitors reveals a time-dependent process of cell fate acquisition in mouse and human nephrogenesis. Dev. Cell 45, 651–660.e4 (2018).
- Prahl, L. S., Viola, J. M., Liu, J. & Hughes, A. J. The developing murine kidney actively negotiates geometric packing conflicts to avoid defects. Dev. Cell 58, 110–120.e5 (2023).
- Irvine, W. T. M., Vitelli, V. & Chaikin, P. M. Pleats in crystals on curved surfaces. *Nature* 468, 947–951 (2010).
- Bausch, A. R. et al. Grain boundary scars and spherical crystallography. Science 299, 1716–1718 (2003).
- Jiménez, F. L., Stoop, N., Lagrange, R., Dunkel, J. & Reis, P. M. Curvature-controlled defect localization in elastic surface crystals. *Phys. Rev. Lett.* 116, 104301 (2016).
- Brojan, M., Terwagne, D., Lagrange, R. & Reis, P. M. Wrinkling crystallography on spherical surfaces. *Proc. Natl Acad. Sci. USA* 112, 14–19 (2015).
- Bowick, M. J. & Giomi, L. Two-dimensional matter: order, curvature and defects. Adv. Phys. 58, 449–563 (2009).

- Davies, J. A., Hohenstein, P., Chang, C.-H. & Berry, R. A self-avoidance mechanism in patterning of the urinary collecting duct tree. BMC Dev. Biol. 14, 35 (2014).
- England, A. R. et al. Identification and characterization of cellular heterogeneity within the developing renal interstitium. Development 147, dev190108 (2020).
- 18. Yao, Z. Stress-induced ordering of two-dimensional packings of elastic spheres. *Phys. Rev. E* **101**, 062904 (2020).
- Liu, A. J. & Nagel, S. R. The jamming transition and the marginally jammed solid. *Annu. Rev. Condens. Matter Phys.* 1, 347–369 (2010).
- 20. Sullivan, J. M. in *Foams and Emulsions* (eds Sadoc, J. F. & Rivier, N.) 379–402 (Springer Netherlands, 1999).
- 21. Honda, H. Description of cellular patterns by Dirichlet domains: the two-dimensional case. *J. Theor. Biol.* **72**, 523–543 (1978).
- Lindström, N. O. et al. Conserved and divergent features of human and mouse kidney organogenesis. J. Am. Soc. Nephrol. 29, 785–805 (2018).
- Princen, H. M. Rheology of foams and highly concentrated emulsions: I. Elastic properties and yield stress of a cylindrical model system. J. Colloid Interface Sci. 91, 160–175 (1983).
- Mongera, A. et al. A fluid-to-solid jamming transition underlies vertebrate body axis elongation. *Nature* 561, 401–405 (2018).
- Mason, T. G., Bibette, J. & Weitz, D. A. Yielding and flow of monodisperse emulsions. J. Colloid Interface Sci. 179, 439–448 (1996).
- Bolton, F. & Weaire, D. Rigidity loss transition in a disordered 2D froth. Phys. Rev. Lett. 65, 3449–3451 (1990).
- 27. Bi, D., Lopez, J. H., Schwarz, J. M. & Manning, M. L. A density-independent rigidity transition in biological tissues. *Nat. Phys.* **11**, 1074–1079 (2015).
- Farhadifar, R., Röper, J.-C., Aigouy, B., Eaton, S. & Jülicher, F.
 The influence of cell mechanics, cell-cell interactions, and
 proliferation on epithelial packing. *Curr. Biol.* 17, 2095–2104
 (2007).
- 29. Park, J.-A. et al. Unjamming and cell shape in the asthmatic airway epithelium. *Nat. Mater.* **14**, 1040–1048 (2015).
- 30. Sussman, D. M. & Merkel, M. No unjamming transition in a Voronoi model of biological tissue. *Soft Matter* **14**, 3397–3403 (2018).
- Merkel, M., Baumgarten, K., Tighe, B. P. & Manning, M. L. A minimal-length approach unifies rigidity in underconstrained materials. *Proc. Natl Acad. Sci. USA* 116, 6560–6568 (2019).
- 32. Sussman, D. M. Interplay of curvature and rigidity in shape-based models of confluent tissue. *Phys. Rev. Res.* **2**, 023417 (2020).
- Scarcelli, G. & Yun, S. H. Confocal Brillouin microscopy for threedimensional mechanical imaging. *Nat. Photon.* 2, 39–43 (2007).
- Handler, C., Scarcelli, G. & Zhang, J. Time-lapse mechanical imaging of neural tube closure in live embryo using Brillouin microscopy. Sci. Rep. 13, 263 (2023).
- 35. Bevilacqua, C. et al. High-resolution line-scan Brillouin microscopy for live imaging of mechanical properties during embryo development. *Nat. Methods* **20**, 755–760 (2023).
- Schlüßler, R. et al. Mechanical mapping of spinal cord growth and repair in living zebrafish larvae by Brillouin imaging. *Biophys. J.* 115, 911–923 (2018).
- Zhang, J. et al. Nuclear mechanics within intact cells is regulated by cytoskeletal network and internal nanostructures. Small 16, 1907688 (2020).
- 38. Rosines, E. et al. Constructing kidney-like tissues from cells based on programs for organ development: toward a method of *in vitro* tissue engineering of the kidney. *Tissue Eng. A* **16**, 2441–2455 (2010).
- Davis, S. N. et al. Nephron progenitors rhythmically alternate between renewal and differentiation phases that synchronize with kidney branching morphogenesis. Preprint at *bioRxiv* https://doi.org/10.1101/2023.11.21.568157 (2023).

- Ishizaki, T. et al. Pharmacological properties of Y-27632, a specific inhibitor of rho-associated kinases. *Mol. Pharmacol.* 57, 976–983 (2000).
- 41. Viola, J. M. et al. Rho/ROCK activity tunes cell compartment segregation and differentiation in nephron-forming niches. Preprint at *bioRxiv* https://doi.org/10.1101/2023.11.08.566308 (2023).
- Kong, W. et al. Experimental validation of force inference in epithelia from cell to tissue scale. Sci. Rep. 9, 14647 (2019).
- 43. Chiou, K. K., Hufnagel, L. & Shraiman, B. I. Mechanical stress inference for two dimensional cell arrays. *PLoS Comput. Biol.* **8**, e1002512 (2012).
- 44. Zulueta-Coarasa, T. & Fernandez-Gonzalez, R. in *Integrative Mechanobiology* (eds Sun, Y. et al.) 128–147 (Cambridge Univ. Press, 2015).
- Volovelsky, O. et al. Hamartin regulates cessation of mouse nephrogenesis independently of Mtor. *Proc. Natl Acad. Sci. USA* 115, 5998–6003 (2018).
- 46. Cebrian, C., Asai, N., D'Agati, V. & Costantini, F. The number of fetal nephron progenitor cells limits ureteric branching and adult nephron endowment. *Cell Rep.* **7**, 127–137 (2014).
- 47. Hoy, W. E., Hughson, M. D., Bertram, J. F., Douglas-Denton, R. & Amann, K. Nephron number, hypertension, renal disease, and renal failure. *J. Am. Soc. Nephrol.* **16**, 2557–2564 (2005).

- 48. Lefevre, J. G. et al. Branching morphogenesis in the developing kidney is governed by rules that pattern the ureteric tree. *Development* **144**, 4377–4385 (2017).
- Lawlor, K. T. et al. Nephron progenitor commitment is a stochastic process influenced by cell migration. *Elife* 8, e41156 (2019).
- Howden, S. E., Vanslambrouck, J. M., Wilson, S. B., Tan, K. S.
 & Little, M. H. Reporter-based fate mapping in human kidney organoids confirms nephron lineage relationships and reveals synchronous nephron formation. *EMBO Rep.* 20, e47483 (2019).

Publisher's note Springer Nature remains neutral with regard to jurisdictional claims in published maps and institutional affiliations.

Springer Nature or its licensor (e.g. a society or other partner) holds exclusive rights to this article under a publishing agreement with the author(s) or other rightsholder(s); author self-archiving of the accepted manuscript version of this article is solely governed by the terms of such publishing agreement and applicable law.

@ The Author(s), under exclusive licence to Springer Nature Limited 2024

Methods

Animal experiments

Mouse protocols followed National Institutes of Health (NIH) guidelines and were approved by the Institutional Animal Care and Use Committee of the University of Pennsylvania. E14–E17 embryos were collected from timed pregnant CD-1 mice (Charles River) and stages confirmed by limb anatomy⁵¹. Embryonic kidneys were dissected in Dulbecco's phosphate buffered saline (DPBS; MT21-31-CV, Corning)⁵².

Whole-mount confocal kidney immunofluorescence imaging

Immunofluorescence staining and imaging was performed using protocols adapted from refs. 10,53,54. Dissected kidneys were fixed in ice-cold 4% paraformaldehyde in DPBS for 20 min and washed three times for 5 min per wash in ice-cold DPBS. Kidneys were then blocked for 2 h at room temperature in PBSTX (DPBS + 0.1% Triton X-100) containing 5% donkey serum (D9663, Sigma) and incubated in primary and then secondary antibodies in blocking buffer at 4 °C, with each of these steps alternating with three washes in PBSTX. The minimum staining duration was 40 h for E14 plus 8 h per additional embryonic day, and for washes, the duration was 12 h for E14 plus 3 h per additional embryonic day (that is, at least 64 h staining and 21 h wash cycles for E17 kidneys) 53 .

Primary antibodies and dilutions included rabbit anti-Six2 (1:600, 11562-1-AP, Proteintech, Research Resource Identifier (RRID) AB_2189084), mouse anti-E-cadherin (E, epithelial; 1:200, clone 34, 610404, BD Biosciences, RRID AB_397787), rat anti-E-cadherin (1:100, ab11512, abcam, RRID AB 298118), mouse anti-calbindin D-28K (1:100, clone CB-955, C9849, Sigma, RRID AB 476894), mouse anti-pancytokeratin(1:200,clone11,C2931,Sigma,RRIDAB_258824)andgoatantijagged 1 (1:150, AF599, R&D Systems, RRID AB 2128257). Secondary antibodies (all raised in donkey) were used at 1:300 dilution and include anti-rabbit Alexa Fluor 647 (A31573, Thermo Fisher, RRID AB 2536183), anti-rabbit Alexa Fluor 555 (A31570, Thermo Fisher, RRID AB_2536180), anti-mouse Alexa Fluor 555 (A31572, Thermo Fisher, RRID AB_162543), anti-goat Alexa Fluor 488 (A11055, Thermo Fisher, RRID AB 2534102), anti-rat Alexa Fluor Plus 555 (A48270, Thermo Fisher, RRID AB 2896336), anti-rabbit Alexa Fluor 488 (A21206, Thermo Fisher, RRID AB_2535792) and anti-rat Alexa Fluor Plus 405 (A48268, Thermo Fisher, RRID AB 2890549). In some experiments, samples were counterstained in 300 nM DAPI (4',6-diamidino-2-phenylindole; D1306, Thermo Fisher), 20 µg ml⁻¹ Alexa Fluor 488-labelled PNA (L21409, Sigma) and/or 1:40 Alexa Fluor 647 phalloidin (A22287, Thermo Fisher) diluted in blocking buffer for 2 h at room temperature, followed by three washes in phosphate buffered saline (PBS).

Kidneys were imaged in wells created with a 2-mm-diameter biopsy punch in an ~5-mm-thick layer of 15:1 (base/crosslinker) polydimethylsiloxane (PDMS) elastomer (Sylgard 184, 2065622, Ellsworth Adhesives) set in 35 mm cover-slip-bottom dishes (FD35-100, World Precision Instruments). Imaging was performed using a Nikon Ti2-E microscope equipped with a CSU-W1 spinning disc (Yokogawa); a white-light light-emitting diode (LED) for transmitted imaging; laser illumination (100 mW 405, 488 and 561 nm lasers and a 75 mW 640 nm laser); a Prime 95B back-illuminated scientific complementary metaloxide—semiconductor (sCMOS) camera (Photometrics); a motorized stage; ×4/0.2 numerical aperture, ×10/0.25 numerical aperture and ×20/0.5 numerical aperture lenses (Nikon); and a Stage Top environmental enclosure (OkoLab). The system was operated under control of NIS-Elements AR software (Nikon, v.5.11.00).

Embryonic kidney data annotation

UB tip positions were manually annotated from confocal stacks in Fiji (ImageJ2, v.2.14.0) using the multi-point tool. Nephrons per tip were manually annotated from confocal stacks of the SIX2 and PNA channels, summing across SIX2+ pre-tubular aggregates or early renal vesicles and later stages for which connecting tubule junctions with UB tips were visible as circular intersections in the PNA channel at tips.

Confocal immunofluorescence stacks on the SIX2 channel were manually annotated to extract kidney outlines at each z plane by manually tracing using the freehand selection tool in Fiji on an Apple iPad. These outlines constituted a binary mask stack used as input to the curvature analysis.

Voronoi, shape index and defect charge analysis

Delaunay triangulations and Voronoi diagrams were created from UB tip coordinates in MATLAB (TheMathWorks, v.R2022a), filtered by polygon area and manually edited to remove Voronoi cells at the edges. The coordination number was determined as the number of sides of each Voronoi cell, and shape index p was determined via $p = P/\sqrt{A}$, where P is the perimeter of a Voronoi cell and A is its area. Heat maps of shape index were produced by interpolation of shape index data in MATLAB using the 'v4' method in griddata.m. The total disclination defect charge Q for a particular Voronoi diagram was determined by summing the topological charges s over all Voronoi cells (note, s = 6 - z, where z is the coordination number of a cell).

Packing model

We used physics-based modelling in Rhino (v.7, Robert McNeel & Associates) Grasshopper Kangaroo2 (Daniel Piker) to demonstrate repulsive sphere packing on flat surfaces and spheres in Fig. 1b and on a kidney surface mesh in Supplementary Video 2 (details are in the section 'Kidney curvature analysis', below). Quantitative principles of this software environment are detailed in ref. 10. We used the Sphere Collide goal to model sphere mutual repulsion and the OnMesh goal to hold spheres at flat or curved interfaces, each with arbitrarily high energy potential weightings to mimic previously described features of particle packings on surfaces (1-13,55). To create overlay schematics, sphere coordinates were exported from Rhino and used as input to the same Voronoi and coordination number analysis performed in MATLAB.

Kidney curvature analysis

The 3D mask stacks of kidney outlines were first exported from the 3D viewer in Fiji as binary .stl meshes representing kidney surfaces (Supplementary Fig. 1). These .stl files were then imported into Rhino, remeshed down to ~1,000 polygons using quad remesh, smoothed, triangulated, draped and split to remove the bottom face. Contour cross-sections were created at 20 μ m increments along the long axis and lofted to create a smooth, regular mesh representing the outer kidney surface. Surface meshes were exported as .stl files, imported into MATLAB and represented as height maps using the stlread and trisurf functions. Exported meshes were also analysed to determine the Gaussian curvature local to each polygon via a custom workflow in Rhino Grasshopper. The area-weighted sum of polygon Gaussian curvature K, $I = \int_A K dA$, over an equivalent area covered by the Voronoi diagram for that surface was then used to compute the integrated Gaussian curvature in units of disclinations, $\Omega = \frac{I}{\pi/3}$.

Spatial autocorrelation analysis

The 2D spatial autocorrelation heat maps of tip regions were computed from maximum projections of confocal *z* stacks on the PNA fluorescence channel using the Wiener–Khintchine theorem in MAT-LAB (autocorr2d function, Tristan Ursell).

Polyacrylamide gels

The 7.5% acrylamide and 0.035, 0.05, 0.07 and 0.15% bis-acrylamide polyacrylamide gels were fabricated as follows 56 . First, to create surfaces that support gel adhesion, standard $1^\prime \times 3^\prime$ microscope slides were cleaned, etched in 1 N sodium hydroxide (NaOH) and coated with a surface layer of 3-(trimethoxysilyl) propyl methacrylate (440159, Sigma) diluted in acetic acid and water. Acrylamide and bis-acrylamide were mixed to appropriate ratios in $\times 1$ PBS ($\times 10$ stock, no. 1420075, Gibco) and degassed under vacuum. Polymerization was initiated by

adding 0.05% (w/v) ammonium persulfate (A3678, Sigma) and 0.05% (v/v) N, N, N, N, N-tetramethylenediamine (T9281, Sigma) and thoroughly mixing. Some 100 μ l of prepolymer mixture was introduced into a ~450 μ m gap between the methacrylate-silanized 'half' glass slide (split in two using a diamond scribe) and a $2' \times 3'$ dichlorodimethylsilane (DCDMS)-treated hydrophobic slide (2947, Corning); the gap was created using triple-layered laboratory tape shims. Polymerization was carried out in a nitrogen-rich atmosphere to reduce the inhibition effects of oxygen, especially at gel boundaries. Gels used in microindentation measurements contained 0.1% (v/v) of 0.2- μ m-diameter far-red fluorescent carboxylate microspheres (FluoSpheres, F8807, Thermo Fisher) in the prepolymer mixture to enable measurement of gel thickness using a confocal fluorescence z stack. Gels used in Brillouin measurements lacked beads.

Brillouin microscopy

A confocal Brillouin microscope was used for acquiring mechanical images of kidneys and polyacrylamide gels⁵⁷. The microscope consisted of a Brillouin spectrometer and a commercial fluorescence microscope (IX83, Olympus). A continuous wave laser (~17 mW, 660 nm, Torus, Laser Quantum) was used as a light source. The laser beam was focused into a spot of 0.7 μ m \times 0.7 μ m \times 2 μ m using a ×40/0.6 objective lens (Olympus). The high-resolution Brillouin spectrometer was built from a two-stage virtually imaged phased array (free spectral range FSR = 15 GHz, LightMachinery). The spectrometer is shot-noise limited and has a spectral precision of 0.01 GHz, suggesting a sensitivity of 0.16% for water-based materials. Brillouin spectra were collected using an electron multiplying charge-coupled device (EMCCD) camera (iXon Life 897, Andor). During the Brillouin experiment, kidney tip domains were scanned at room temperature with a step size of 1 µm and an acquisition speed of 50 ms per point. UB epithelium tip PNA fluorescence was also imaged on a separate channel to later register with the corresponding Brillouin images. The longitudinal modulus (M') is determined by the measured Brillouin shift (v_B) via the relationship $M' = v_B^2 \times \lambda^2 \times \rho/4n^2$, where λ is the wavelength of the laser and n and ρ are the refractive index and density of the sample, respectively. To calculate the longitudinal modulus, we estimated n = 1.40 from literature measurements of the adult kidney⁵⁸. The density was calculated as 1.096 g ml⁻¹ based on a published relationship between refractive index and density for biological materials³⁶. According to the linear log-log relationship between longitudinal modulus (M') and Young's modulus (E), the relative changes of both moduli are related by $\Delta E/E = (1/a) \times \Delta M'/M'$, where the coefficient a = 0.0671 was obtained by calibration with an atomic force microscope using NIH 3T3 cells³⁷.

For polyacrylamide gels, a 12 mW laser power was used during Brillouin measurement. Multiple locations on each sample were measured, and the averaged value was used to represent the overall Brillouin shift of the sample. To calculate the longitudinal modulus, the densities of the gels were estimated based on the concentrations of acrylamide and bis-acrylamide in water, with the refractive index approximated as 1.33 (ref. 59).

Microindentation

Free-standing mouse kidneys were microindented immediately after dissection⁶⁰. Instrumentation was the same as described in ref. 60, except the indenter arm height was controlled by a stepper motor (L4018S12O4-M6, Nanotec) rather than a hydraulic micromanipulator. The indenter was fabricated from cylindrical 30 gauge (American Wire Gage, AWG) SAE 316L stainless steel wire having a diameter of 255 µm. Briefly, after calibrating the spring constant of the tensiometric sensor, each kidney was placed in a 35 mm culture dish and bulk media wicked away to leave the kidney surface semi-dry. The indenter was immediately lowered at a rate of 12.5 µm s⁻¹ using the z stage of the instrument to an indentation depth of ~30 µm into the

kidney surface while automatically recording the time, force on the indenter and indenter z position. Indentation was then halted and force versus time recorded for an additional 60–120 s. Poles from the same kidneys were indented after bisecting kidneys with a razor blade and facing them pole-side up. Polyacrylamide gels were indented as previously described 56 . Stiffness was inferred using the following relationship for the indentation of a soft homogeneous material by a flat hard surface:

$$E_{\text{tissue}} = \frac{F_{\text{appl}}(1 - v_{\text{tissue}}^2)}{h_{\text{ind}} \kappa 2r}$$

where $F_{\rm appl}/h_{\rm ind}$ is the slope of force versus indentation depth from the point of contact after accounting for sensor spring constant; $v_{\rm tissue}$ is the Poisson ratio of the tissue, assumed to be 0.5; κ is the Hayes correction factor of, accounting for finite sample thickness (κ was determined for each whole kidney stage based on the average kidney/pole width inferred from confocal image stacks, and for polyacrylamide gels based on confocal image stacks); and 2r is the diameter of the probe (255 µm).

Similar to previous analysis 60 , force versus time (t) traces at fixed indentation depth were normalized to maximum force and fit to the following three-parameter relaxation relationship using nonlinear least-squares fitting in MATLAB (the lsqcurvefit function):

$$F_{\text{norm}} = 1 - (1 - G_{\infty})(1 - e^{-t/\tau}) - kt.$$

This relationship implies a Kelvin–Voigt material with an extra viscous damper in series, where G_{∞} and τ are an equilibrium modulus and relaxation time constant, respectively. We refer to k as a viscous relaxation constant in this work. For the fits underlying the data presented in Fig. 3d,e, errors in parameter estimates were determined using the nlparci function in MATLAB. Stated in terms of coefficients of variation relative to the fitted parameter values (s.d./value × 100), these were $0.20 \pm 0.17\%$ (mean \pm s.d.) with a maximum of 0.82% for G_{∞} , $1.2 \pm 0.79\%$ with a maximum of 3.3% for τ and $0.97 \pm 1.0\%$ with a maximum of 5.8% for k.

Nuclear aspect ratio and stromal ribbon cell alignment relative to tip domain interfaces

Cell nuclei were manually annotated at the indicated z depths in whole-mount confocal immunofluorescence z stacks. Stromal cells were annotated on the MEIS1/2 channel, and cap mesenchyme nephron progenitors were annotated on the SIX2 channel. Annotations were made by manual tracing in Fiji using the freehand selection tool on an Apple iPad. Aspect ratio and angular orientation metrics were outputted from Fiji for fitting ellipses of each nuclear mask. The angle of each nuclear mask relative to the closest tip domain Voronoi boundary was then determined by manually associating nuclear masks to boundaries and calculating their angular deviation.

Force inference

Tip domain Voronoi diagrams were segmented in the Tissue Analyzer plugin in Fiji (ref. 62) and output data were passed to MATLAB for Bayesian force inference using code published by Kong et al. ^{42,63}. We used this code to compute stress tensors and their isotropic and anisotropic components for each tip domain using Batchelor's formula ^{42,63}:

$$\sigma_{\mu\nu} = \left(-\sum_{i=\text{domains}} P_i a_i \delta_{\mu\nu} + \sum_{|ij|=\text{interfaces}} \frac{T_{ij} l_{ij}^{\mu} l_{ij}^{\nu}}{\|l_{ij}\|}\right) / \sum_{i=\text{domains}} a_i$$

where a_i is the area of domain i, P_i is its pressure, δ is Kronecker's symbol, T_{ij} is the tension of the interface i–j separating domains i and j and $\mathbf{l}_{ij} = (I_{ij}^{\kappa}, I_{ij}^{\nu})$ is the vector connecting the two vertices of interface i–j. μ and ν are indices for x and y.

The resulting stress tensor σ can be considered to be a combination of isotropic and anisotropic parts, that is $\sigma = \sigma_{\rm iso} I + \sigma'$, where $\sigma_{\rm iso}$ is the isotropic stress, I is the identity matrix and σ' is the anisotropic (deviatoric) stress tensor. The σ can be drawn as bars representing principal (maximum and minimum) normal stresses along their eigenvectors (principal directions), with lengths proportional to their eigenvalues (magnitudes) λ_1 and λ_2 (ref. 42). The anisotropic stress tensor can be similarly drawn as one bar representing tension, since the orthogonal bar of equal magnitude in compression is redundant⁶⁴. We can summarize the isotropic part of the stress as $(\lambda_1 + \lambda_2)/2$ and the anisotropic part as $|\lambda_1 - \lambda_2|$ (refs. 63,64). Since stress outputs are relative here, we normalized them to the largest median stress in a given set of shape index group comparisons.

Laser ablation

Freshly dissected E15 and E17 kidneys were labelled in 20 µg ml⁻¹ Alexa Fluor 488-labelled PNA and 1:1,000 CellTracker Red (Thermo Fisher C34552, 10 mM stock in dimethyl sulfoxide) in Dulbecco's minimum essential medium (DMEM, 10-013-CV, Corning) for 1 h at 37 °C, washed three times in DMEM and placed in 2-mm-diameter PDMS wells (details in the section 'Whole-mount confocal kidney immunofluorescence imaging'), this time plasma bonded to a quartz cover-slip (no. 1 thickness, Ted Pella, 26014) to maximize UV transmission. In some experiments, kidneys were incubated for 4 h with 30 μM ROCKi Y-27632 in DMEM or in DMEM without ROCKi as an incubated control prior to PNA and CellTracker labelling and ablation. Kidneys were ablated using a 355 nm UV laser (Molecular Machines & Industries, MMI, SL μCut v.1.0) through a ×10 objective on a Nikon Eclipse TE2000-S controlled by MMI software with a Sony DXC-390P three-CCD digital signal processing camera (resolution of 1.1 µm per pixel under experiment conditions). Cut opening time-lapses were imaged from the microscope monitor using a tripod-mounted iPhone 8 (Apple) video camera and spatially calibrated using fiducial marks in the MMI software. Microscope camera output was spatially and temporally super-sampled sevenfold and tenfold, respectively, using this approach. The microscope data collection frame rate was 3 Hz (0.33 s period), giving sufficient resolution to capture recoil time constants τ , which were in the range of 4-20 s. Intensity and spatial calibration target patterns were displayed in Microsoft Paint software (Microsoft Corporation, v.5.1) on the laser-capture microdissection system screen and recorded in the same manner as ablation data. Spatial calibration targets were manually segmented in Fiji and plotted against nominal dimensions. Cut fluorescence traces were nonlinear least-squares fit using the fit function in MATLAB at each time-lapse frame with Gaussians of the form

$$a - be^{-\left(\frac{x-c}{d}\right)^2}$$

where a is fluorescence background, b is magnitude, c is spatial shift and $d = \sqrt{2}\sigma$ in terms of standard deviation σ . Spatial resolution conditions translated to ~30 microscope camera-level data points per Gaussian fit, contributing to fit R^2 values being typically >0.95.

Cut opening width was taken to be the width of the Gaussian at 10% of maximum:

$$L = 2\sqrt{-2\ln(0.1)}\sigma.$$

Cut opening width trajectories were nonlinear least-squares fit with the Kelvin–Voigt model equation⁴⁴ using the Isqcurvefit function in MATLAB:

$$L(t) - L(0) = D\left(1 - e^{-\frac{t}{\tau}}\right)$$

where L(0) and L(t) are cut opening widths at time zero and time t, respectively; D is the asymptotic cut opening distance; and τ is a time

constant. Errors in parameter estimates stated in terms of coefficients of variation relative to the fitted parameter values were determined using the nlparci function.

Kidneys were fixed after ablations in ice-cold 4% paraformaldehyde for 15 min, washed three times with PBS and imaged by confocal microscopy (details are in the section 'Whole-mount confocal kidney immunofluorescence imaging').

Statistics and reproducibility

Measurements were collected from 2–3 separate experiments (biological replicates) in cases where representative data are presented. Sample size (n) and statistical tests are noted in figure legends. One-way ANOVA with correction for multiple comparisons using Tukey's honestly significant difference test was performed in MATLAB using the anoval and multcompare functions. Paired and unpaired t-tests were performed in MATLAB using the ttest and ttest2 functions, respectively.

Reporting summary

Further information on research design is available in the Nature Portfolio Reporting Summary linked to this article.

Data availability

All data necessary to evaluate the conclusions of this study are presented in the paper and Supplementary Information. Raw image stacks are available upon request due to prohibitive file sizes. Source data are available via Github at https://github.com/ahug030/kidney_jamming.

Code availability

Code used to generate curvature and height maps, Voronoi networks and shape index data, and sphere packing simulations is available at https://github.com/ahug030/kidney_jamming.

References

- 51. Wanek, N., Muneoka, K., Holler-Dinsmore, G., Burton, R. & Bryant, S. V. A staging system for mouse limb development. *J. Exp. Zool.* **249**, 41–49 (1989).
- Barak, H. & Boyle, S. C. Organ culture and immunostaining of mouse embryonic kidneys. *Cold Spring Harb. Protoc*. https://doi.org/10.1101/pdb.prot5558 (2011).
- 53. Combes, A. N. et al. An integrated pipeline for the multidimensional analysis of branching morphogenesis. *Nat. Protoc.* **9**, 2859–2879 (2014).
- O'Brien, L. L. et al. Wnt11 directs nephron progenitor polarity and motile behavior ultimately determining nephron endowment. *Elife* 7, e40392 (2018).
- 55. Negri, C., Sellerio, A. L., Zapperi, S. & Miguel, M. C. Deformation and failure of curved colloidal crystal shells. *Proc. Natl Acad. Sci. USA* **112**, 14545–14550 (2015).
- Prahl, L. S., Porter, C. M., Liu, J., Viola, J. M. & Hughes, A. J. Independent control over cell patterning and adhesion on hydrogel substrates for tissue interface mechanobiology. iScience 26, 106657 (2023).
- 57. Zhang, J. & Scarcelli, G. Mapping mechanical properties of biological materials via an add-on Brillouin module to confocal microscopes. *Nat. Protoc.* **16**, 1251–1275 (2021).
- Bolin, F. P., Preuss, L. E., Taylor, R. C. & Ference, R. J. Refractive index of some mammalian tissues using a fiber optic cladding method. Appl. Opt. 28, 2297–2303 (1989).
- Hariri, A. et al. Polyacrylamide hydrogel phantoms for performance evaluation of multispectral photoacoustic imaging systems. *Photoacoustics* 22, 100245 (2021).
- Levental, I. et al. A simple indentation device for measuring micrometer-scale tissue stiffness. J. Phys. Condens. Matter 22, 194120 (2010).

- Hayes, W. C., Keer, L. M., Herrmann, G. & Mockros, L. F. A mathematical analysis for indentation tests of articular cartilage. *J. Biomech.* 5, 541–551 (1972).
- Aigouy, B., Umetsu, D. & Eaton, S. Segmentation and quantitative analysis of epithelial tissues. *Methods Mol. Biol.* 1478, 227–239 (2016).
- 63. Ishihara, S. & Sugimura, K. Bayesian inference of force dynamics during morphogenesis. *J. Theor. Biol.* **313**, 201–211 (2012).
- 64. Guirao, B. et al. Unified quantitative characterization of epithelial tissue development. *Elife* **4**, e08519 (2015).

Acknowledgements

We thank the Hughes lab members Z. Gartner, C. Nelson and M. Little for discussions and advice. We are grateful to K. Bennett at the Molecular Pathology and Imaging Core, Gastroenterology Division, Penn Medicine for technical assistance with laser ablation studies; and D. Li and P. Janmey for access to and training on microindentation. We thank N. Lindström for sending the supplementary image files from ref. 22. This work was supported by the following: NIH F32 fellowship DK126385 and Penn Center for Soft & Living Matter fellowship (L.S.P.), the Predoctoral Training Program in Developmental Biology T32HD083185 (J.M.V.), National Science Foundation (NSF) Graduate Research Fellowship Program (GRFP; J.L., T.J.C., G.H.-L. and C.M.P.), NIH National Institute of Child Health and Human Development (NICHD) K25HD097288 (J.Z.), NIH NICHD R21HD112663 (J.Z.), NIH National Institute of General Medical Sciences (NIGMS) Maximizing Investigators' Research Award (MIRA) R35GM133380 (A.J.H.), NIH National Institute of Diabetes and Digestive and Kidney Diseases (NIDDK) R01DK132296 (A.J.H.) and NSF CAREER awards 2339278 (J.Z.) and 2047271 (A.J.H.).

Author contributions

Conceptualization was by L.S.P., J.M.V., T.J.C. and A.J.H. Methodology was by L.S.P., J.L., J.M.V., A.H., T.J.C., G.H.-L., C.M.P., J.Z. and A.J.H. Software was by J.M.V., T.J.C., J.Z. and A.J.H. Formal analysis was by J.M.V., T.J.C., J.Z. and A.J.H. Investigation was by L.S.P., J.L., J.M.V., A.H., T.J.C., G.H.-L., C.M.P., C.S., J.Z. and A.J.H. Writing the original draught was by J.Z. and A.J.H. Reviewing and editing was by L.S.P., J.L., J.M.V., A.H., T.J.C., G.H.-L., C.M.P., J.Z. and A.J.H. Visualization was by L.S.P., J.M.V., T.J.C., G.H.-L., C.S., J.Z. and A.J.H. Supervision was by L.S.P., J.Z. and A.J.H. Project administration was by J.Z. and A.J.H.

Competing interests

L.S.P., J.M.V., J.L., A.H., C.M.P. and A.J.H. are listed as co-inventors on a published University of Pennsylvania international patent (WO 2023/235828 A1) relating to mechanics of nephrogenesis.

Additional information

Supplementary information The online version contains supplementary material available at https://doi.org/10.1038/s41563-024-02019-3.

Correspondence and requests for materials should be addressed to Alex J. Hughes.

Peer review information *Nature Materials* thanks Nuria Montserrat and the other, anonymous, reviewer(s) for their contribution to the peer review of this work.

Reprints and permissions information is available at www.nature.com/reprints.

nature portfolio

Corresponding author(s):	Alex Hughes
Last updated by author(s):	July 12, 2024

Reporting Summary

Nature Portfolio wishes to improve the reproducibility of the work that we publish. This form provides structure for consistency and transparency in reporting. For further information on Nature Portfolio policies, see our Editorial Policies and the Editorial Policy Checklist.

For all statistical analyses, confirm that the following items are present in the figure legend, table legend, main text, or Methods section.

\sim			
۲	at	101	tics

n/a	Confirmed
	\square The exact sample size (n) for each experimental group/condition, given as a discrete number and unit of measurement
	🔀 A statement on whether measurements were taken from distinct samples or whether the same sample was measured repeatedly
	The statistical test(s) used AND whether they are one- or two-sided Only common tests should be described solely by name; describe more complex techniques in the Methods section.
\boxtimes	A description of all covariates tested
	A description of any assumptions or corrections, such as tests of normality and adjustment for multiple comparisons
	A full description of the statistical parameters including central tendency (e.g. means) or other basic estimates (e.g. regression coefficient) AND variation (e.g. standard deviation) or associated estimates of uncertainty (e.g. confidence intervals)
	For null hypothesis testing, the test statistic (e.g. <i>F</i> , <i>t</i> , <i>r</i>) with confidence intervals, effect sizes, degrees of freedom and <i>P</i> value noted <i>Give P values as exact values whenever suitable.</i>
\boxtimes	For Bayesian analysis, information on the choice of priors and Markov chain Monte Carlo settings
\boxtimes	For hierarchical and complex designs, identification of the appropriate level for tests and full reporting of outcomes
\boxtimes	Estimates of effect sizes (e.g. Cohen's <i>d</i> , Pearson's <i>r</i>), indicating how they were calculated
	Our web collection on statistics for biologists contains articles on many of the points above.

Software and code

Policy information about availability of computer code

Data collection

Commercial: Nikon Elements (vAR 5.11.00) was used to acquire immunofluorescence image stacks, Molecular Machines & Industries software (v1.0) was used to perform laser cutting, and Microsoft Paint (v5.1) was used to calibrate screen capture data from laser cutting experiments. Other custom codes/GUIs were used in Brillouin microscopy and micro-indentation data collection.

Data analysis

Commercial: MATLAB R2022a, Rhino 7. Open Source: FIJI v1.0 (ImageJ2 v2.14.0), Bayesian force inference code published by Kong et al. (see Methods), Kangaroo2. Other custom codes/GUIs were used in Voronoi analysis, curvature and shell height calculation/representation, shape index maps, see Methods for details. Code is available at https://github.com/ahug030/kidney_jamming.

For manuscripts utilizing custom algorithms or software that are central to the research but not yet described in published literature, software must be made available to editors and reviewers. We strongly encourage code deposition in a community repository (e.g. GitHub). See the Nature Portfolio guidelines for submitting code & software for further information.

Data

Policy information about availability of data

All manuscripts must include a data availability statement. This statement should provide the following information, where applicable:

- Accession codes, unique identifiers, or web links for publicly available datasets
- A description of any restrictions on data availability
- For clinical datasets or third party data, please ensure that the statement adheres to our policy

All data necessary to evaluate conclusions of this study are presented in the paper and supporting information. Raw image stacks are available upon request due to prohibitive file sizes. Source data files are available at https://github.com/ahug030/kidney_jamming.

Research involving human participants, their data, or biological material

Policy information about studies with <u>human participants or human data</u>. See also policy information about <u>sex, gender (identity/presentation), and sexual orientation</u> and <u>race, ethnicity and racism</u>.

Reporting on sex and gender	N/A
Reporting on race, ethnicity, or other socially relevant groupings	N/A
Population characteristics	N/A
Recruitment	N/A
Ethics oversight	N/A

Note that full information on the approval of the study protocol must also be provided in the manuscript.

Field-specific reporting

Please select the one belo	w that is the best fit for your research.	If you are not sure, read the appropriate sections before making your selection.
∠ Life sciences	Behavioural & social sciences	Ecological, evolutionary & environmental sciences

For a reference copy of the document with all sections, see nature.com/documents/nr-reporting-summary-flat.pdf

Life sciences study design

All studies must disclose on these points even when the disclosure is negative.

Sample size	Sample size is typically set by animal and embryo availability per experiment day.	
Data exclusions	No data were excluded from the analysis.	
Replication	Experiments were replicated or pooled among kidneys depending on experiment requirements. Replicate information is stated for each experiment in the figure legends.	
Randomization	Sample allocation was random.	
Blinding	Investigators were not blinded to group allocation during data collection and/or analysis since both were typically performed by the same researcher and since analysis generally ran into tens of hours to days per experiment. Automated analysis was used wherever possible to reduce potential for bias.	

Reporting for specific materials, systems and methods

We require information from authors about some types of materials, experimental systems and methods used in many studies. Here, indicate whether each material, system or method listed is relevant to your study. If you are not sure if a list item applies to your research, read the appropriate section before selecting a response.

Materials & experime	ntal systems	Methods
n/a Involved in the study	r	n/a Involved in the study
Antibodies		ChIP-seq
Eukaryotic cell lines		Flow cytometry
Palaeontology and a	archaeology	MRI-based neuroimaging
Animals and other of		— —
Clinical data		
Dual use research o	f concern	
Plants	redirectif	
MILI Flatits		
Antibodies		
Antibodies used	Primary antibodies and dilutions included rabbit anti-Six2 (1:600, 11562-1-AP, Proteintech, RRID: AB_2189084), mouse anti-Ecadherin (1:200, clone 34, 610404, BD Biosciences, RRID: AB_397787), rat anti-E-cadherin (1:100, ab11512, abcam, RRID:AB_298118), mouse anti-calbindin D-28K (1:100, clone CB-955, C9849, Sigma, RRID: AB_476894), mouse anti-pan-cytokeratin (1:200, clone 11, C2931, Sigma, RRID:AB_258824), and goat anti-jagged 1 (1:150, AF599, R&D Systems, RRID: AB_2128257). Secondary antibodies (all raised in donkey) were used at 1:300 dilution and include anti-rabbit AlexaFluor 647 (A31573, ThermoFisher, RRID: AB_2536183), anti-rabbit AlexaFluor 555 (A31570, ThermoFisher, RRID: AB_2536180), anti-mouse AlexaFluor 555 (A31572, ThermoFisher, RRID: AB_162543), anti-goat AlexaFluor 488 (A11055, ThermoFisher, RRID: AB_2534102), anti-rat AlexaFluor Plus 555 (A48270, ThermoFisher, RRID: AB_2896336), anti-rabbit AlexaFluor 488 (A21206, ThermoFisher, RRID: AB_2535792), and anti-rat AlexaFluor Plus 405 (A48268, ThermoFisher, RRID: AB_2890549). Other counterstains included 1:40 AlexaFluor 647 phalloidin (A22287, ThermoFisher) and 20 μg ml-1 AlexaFluor 488-labeled peanut (Arachis hypogaea) agglutinin lectin (PNA, L21409, Sigma).	
Validation	Antibodies were used in this study to provide anatomical contrast in whole-mount immunofluorescence assays. Antibodies gave signal consistent with previous understanding of developing kidney anatomy and use in previous publications (Prahl et al., Developmental Cell, 2023; Lindstrom et al., Journal of the American Society of Nephrology, 2018; O'Brien et al., eLife, 2018; Combes et al., Nature Protocols, 2014; Short et al., Developmental Cell, 2014). Other validation data is available at vendor websites.	
Animals and othe	r research organis	sms
Policy information about <u>st</u> Research	udies involving animals; ARI	RIVE guidelines recommended for reporting animal research, and <u>Sex and Gender in</u>
Laboratory animals	stages were confirmed by lim	ed from wild-type timed pregnant CD-1 mice (Charles River Laboratories, RRID:IMSR_CRL:022) and b anatomy. Mice were housed in standard ventilated cages (single occupancy) in a conventional rodent lumidity, with free access to water and food and kept on a 12 hour light cycle. Pregnant breeders were
Wild animals	No wild animals were used in	this study.
Reporting on sex		ut regard to embryo sex. Sexual dimorphism appears to be small for a range of anatomical features in ort & Smyth, Scientific Reports, 2015). We treated sex as one contributor to experimental variability in
Field-collected samples	No field-collected samples we	ere used in this study.
Ethics oversight	Mouse protocols followed National Institutes of Health guidelines and were approved by the Institutional Animal Care and Use Committee of the University of Pennsylvania (protocol # 80700).	
Note that full information on t	he approval of the study protoc	col must also be provided in the manuscript.
Dlants		
Plants		
Seed stocks	N/A	
Novel plant genotypes	N/A	
Authentication	N/A	